Nanoscale

Accepted Manuscript

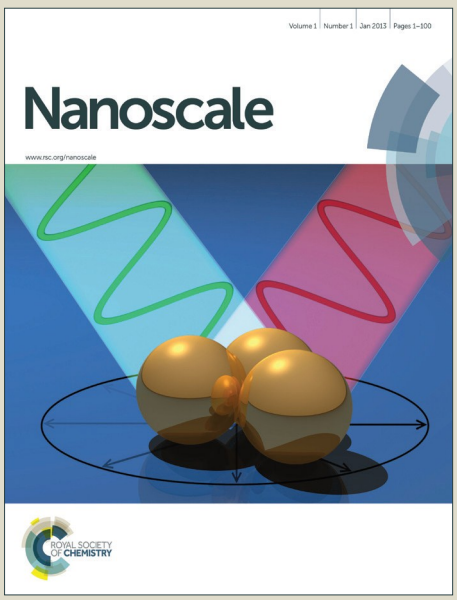

ROYAL SOCIETY OF CHEMISTRY

www.rsc.org/nanoscale

Nanoscale

RSCPublishing

ARTICLE

Graphene nanomesh photodetector with effective charge tunnelling from quantum dots

Cite this: DOI: 10.1039/xoxxooooox

Xiang Liu[a, b]†, Nianze Liu[a]†, Mingju Liu[b], Zhi Tao[a], Wenjian Kuang[a], Xiangbing Ji[a], Jing Chen[a], Wei Lei[c*], Qing Dai[b*], Chi Li[b*], Xuehua Li[a], Arokia Nathan[b]

Received ooth December 2014,
Accepted ooth January 2015

DOI: 10.1039/xoxxooooox

www.rsc.org/

Graphene nanomesh (GNM)-based optoelectronics integrated with quantum dots(QDs) is investigated in this article. The charge transfer mechanism in the QDs/GNM interface is probed in the four terminals gated FET-type photodetectors. And the insulating ligand was used to make the GNM/ligand/QDs vertically behave like a metal/insulate/semiconductor (MIS) structure to facilitate the charge tunnelling. With the current constraint effect of the GNM and the effective charge tunnelling, a high-performance photodetector is fabricated with higher responsivity, higher on/off ratio and shorter response time. Our analysis result and experimental approach can be extended to future Graphene-based photodetectors as long as suitable ligands or effective device architecture is chosen for this kind of device.

1. Introduction

Graphene-based photodetectors, as highly desired devices for various applications from telecommunication, biological imaging to remote sensing[1-4], are regarded as atomic layer two-dimensional (2D) material featuring unprecedented electric and optical properties[5-7]. Especially, based on the research of the graphene-based photodetector, many recent works concentrated on increasing the responsivity, response (measured) time and operation wavelength. To overcome the low responsivity[8-9] of pristine graphene (<0.1 A/W) under illumination of the incident light, ingenious device structures have been proposed in previous reported papers: field effective transistors (FET) device with graphene-quantum dots (QDs) hybrid channel obtains higher responsivity but sacrifices the measurement speed[10]; waveguide graphene photodetectors with special micro-nanostructure accelerate the response speed with a relatively high responsivity over 0.1 A/W[11, 12]; reduced graphene oxide phototransistors featuring defect and atomic structure control outperform pristine graphene devices in terms of photoresponses at the cost of response rate[8]; and some other devices like those with metallic or graphene plasmonic[13-15] micro-nanostructure also attract interests of researchers all over the world immensely.

However, regardless which photo-sensing architectures are chosen to compose the photodetectors, the dynamic charge transfer or energy transfer between the graphene and active components (such as QDs, silicon) [16-17] would always occur in the photo-sensing region. If specialized discussion is carried out in the graphene-QDs hybrid material system, many problems in the interface between graphene and QDs emerge, since the excited QDs need to transfer the electrons or holes to the graphene. To explore those problems from graphene photodetectors, many research groups around the world utilized the specific structure of gated graphene FET transistors to manipulate the charge transfer between graphene and QDs driven by the gate bias and achieved high photosensitivity, high responsivity and broad response waveband[18].

Due to the offset work function between graphene and QDs material, the shottky barrier between QDs and graphene can hinder the direct charge transport from QDs to graphene. In fact, without the bonding of the ligand in QDs surface, the QDs cannot be decorated on the graphene interface[19] steadily. Nevertheless, more-recent reported papers on this type of photodetectors ignored this factor or just chose an electroactive ligand simply without evaluating the charge transfer efficiency or mechanism in this process. Thus, different charge transfer mechanisms are explored deeply in this paper to optimize the fabrication process, material selection and operation performance of the graphene-QDs hybrid photodetectors.

The absence of bandgap in graphene is another damper due to the extent to which the dark current is so high and the on/off ratio[20] (about 1~3) is so low that even the noise photocurrent occurred in the test will considerably interfere the experimental result. As a result, it is difficult to contrast the charge transfer efficiency differences between the QDs with various ligands. Consequently, nanomesh structure was employed in the graphene to open the bandgap and constrain the dark (leakage) current [21].

Finally in this work, excited charges induced by incident light in n-type semiconductor CdSe QDs effectively tunnels through insulating ligand (it is thought to be ineffective for charge transfer in many previous papers) to graphene nanomesh (GNM) channel, which behaves like a MIS (metal-insulate-semiconductor)[22, 23] structure vertically due to the enhanced electric field intensity caused by the bottom gate voltage. It is worth to believe that it will pace a solid step toward the future application of the graphene-based photodetectors with the optimization of the charge transfer efficiency in channel of the FET-type photodetectors.

2. Result and discussion

2.1 Characterization of the GNM FET device

2.1.1 Schematic of the GNM FET device fabrication process and the morphology of the GNM channel. The abbreviated cross-sectional fabrication process flow is depicted in fig. 1a which describes the two main steps: the formation of the GNM and then the bonding between GNM and QDs with different ligand. The width of the graphene nanoribbon in GNM is approximately 20nm (GNM can be treated as graphene nanoribbon networks which is shown in fig. 1c) by using aluminium-anode-oxide (AAO) Membrane mask (shown in fig.1a and b). To investigate the formed GNM, Raman spectra measurement (Fig. 1e) was utilized to ensure that, compared with the pristine graphene, GNM in our work is a typical p-type graphene[20, 24, 25] resulted from the ambient oxidation of the graphene nanoribbon and the influence of the etching process. In addition, Fig. 1d illustrates the 20/200μm Channel (1:10 W/L ratio) of the FET device and inset image show the morphology of the QDs (4.8nm diameter, 590nm peak emission shown in fig. 2c and fig. S1) decorated GNM in the FET channel. In addition, the encapsulated ligand outside the QDs is unstable without any treatment which will cause the decrease of the photo-absorption and charge transfer capability. Thus the approximately 25nm thick QDs layer was bonded on the channel through an annealed process, which can be illustrated in AFM image of fig. 2d. Herein annealing process is essential to form a stable ligand layer with a colloidal morphology which can benefit the formation of the coordination bond between GNM and conjugated organic shell of QDs. The typical annealed effect toward TOPO ligand is also investigated in fig. S4a.

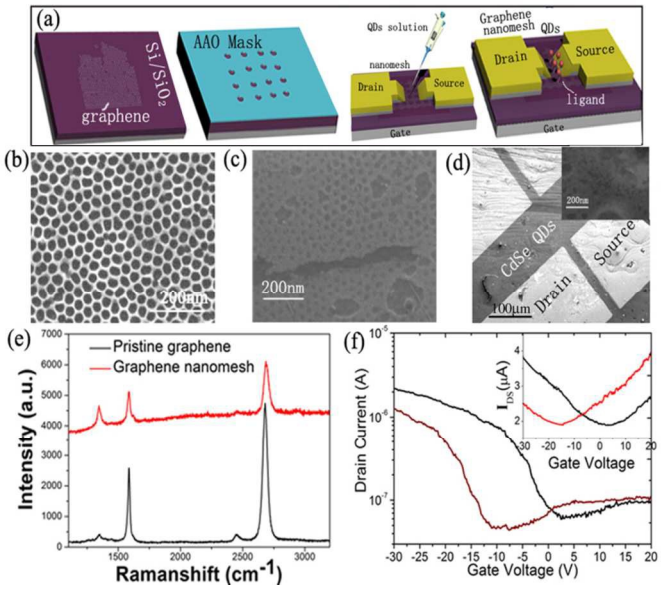

Fig.1 Characterization of the GNM/QDs photodetectors. (a) Cross-sectional abbreviated fabrication process flow of the GNM/QDs photodetectors. (b) SEM image of the AAO mask. (c) GNM morphology after the etching treatment and remove of the AAO mask. (d) A SEM image of the FET device channel and the QDs decorated GNM. (e) The Raman spectrum of pristine graphene and GNM. (f) Transfer characteristic curve of GNM and GNM/QDs(TOPO) FET and that of pristine graphene FET(inset) for V_{DS}=30mV.

2.1.2 Transfer characteristic curve of the pristine graphene/ graphene-QDs hybrid and pristine GNM/GNM-QDs hybrids. The effects of the GNM channel and deposition of QDs on the FET's transfer character are shown in fig. 1f. Firstly, herein, the p-type semiconductor behaviour can be observed which is corresponding to previous investigation of the Raman spectrum[26]. Secondly, according to reported papers[27], the bandgap of 2D graphene is predicted to even reach 200 meV under some certain ambient conditions through the constraints of the narrow graphene nanoribbon which will exhibit a higher on/off ratio. As depicted in fig. 1f, on/off ratio of the as-fabricated FET photodetector is about 30 in our work. Besides on/off current ratio, another trend of the Dirac point blue shift is also demonstrated in the fig. 1f induced by the deposition of the QDs. The doping of the n-type semiconductor CdSe QDs (which has a 4.2-4.3 eV work function) is the main reason of n-doping in GNM channel since work function of graphene is about 4.6eV.

2.2 Photoelectric trigger characteristics of the GNM photodetectors.

2.2.1 Photoluminescent(PL) decay measurement and mechanism of the charge transfer without bottom gate voltage. The electron transfer between QDs and graphene through ligand can be monitored by utilizing transient PL decay spectroscopy. Under 444nm incident laser, the four QDs@ligand samples (as shown in fig.2c and fig.S1 a, b and c) on the GNM silica substrate (fig. 2d) was bonded onto the detection to measure the lifetime variation which can be used to probe the PL quenching effect.

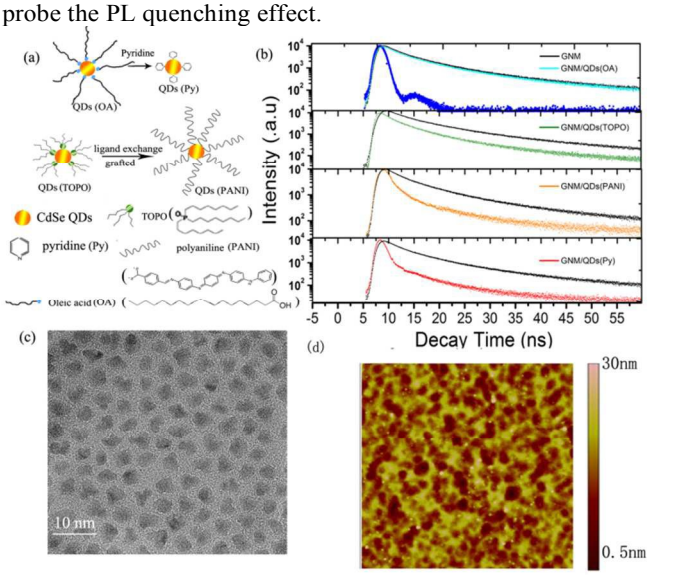

Fig.2 (a) Molecular structures of as-prepared QDs capped with four different ligand and the schematic diagram of the ligand exchange from QDs (TOPO) to QDs capped with electroactive ligands (QDs (Py) and QDs (PANI)). (b) Time-resolved PL decay spectra for pristine GNM interface blended with QDs(OA), QDs(TOPO), QDs(PANI), QDs(Py). (c) The TEM image of well-dispersed QDs(OA) solution. (d) The AFM image of deposited QDs films bonded to graphene channel after annealing.

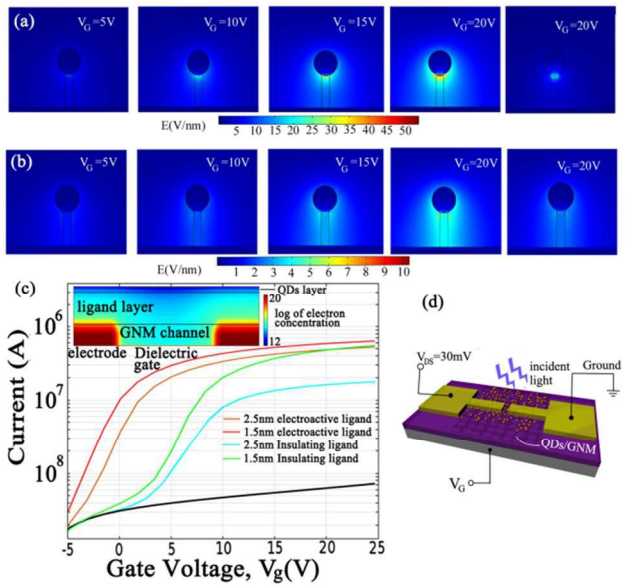

Fig.3 Simulated enhanced built-in electric field in GNM/electroactive-ligands/QDs (a) and MIS structure of insulating ligands (b) for (left to right) Vg=5V, 10V, 15V, 20V and in darkness(20V). (c) The simulated transfer I_D-V_g curve of the GNM/ligand/QDs FET device for V_{DS}=5mV and the log distribution image of electron concentration (inset). (d) The schematic image of the GNM/QD FET photodetector testing circuit.

According to the steady-state PL decay spectra in fig. 2b, QDs capped with electroactive ligands showed a stronger PL quenching substantial compared with the QDs capped with insulating ligands. With less defects, shorter molecular structure (fig. 2a) and better electric conductivity, it seems plausible that only such electroactive ligand as pyridine and PANI facilitates the charge transport from QDs to graphene in the graphene/QDs hybrid system, attesting to the similar results reported in previous papers[19, 28-31], while, on the other side, insulating ligand (such as OA) has no ability to transfer the charge carrier efficiently[10, 19]. However, the weak charge transfer from QDs within insulating ligand (in case of TOPO and OA) may simply be caused by a weak built-in field in the excited-QDs/graphene hybrid interface that cannot supply for the ligand a sufficient tunnelling ability due to the lack of external gate bias. It is likely that, when the gate bias is large enough to enable a considerable tunnelling process, insulating ligands are also able to facilitate the charge transfer considerably.

To better illustrate the hypothesis ab initio, electric field intensity (E, V/nm) distribution of the nanostructure device was simulated by the finite element method (FEM) using COMSOL Multiphysics (v. 3.5a). As shown in fig. 3a and b, with the gate bias set from 5V, 10V, 15V to 20V, the electric field intensity distribution was calculated to predict the GNM/QDs device operation. In the case of small gate voltage (5V and 10V) or non-gate voltage under illumination, the electric field density in insulating ligand device is similar to that in electroactive ligand device. Nevertheless, the uniform electric field intensity distribution in electroactive ligand will benefit the charge transport from QDs, as proved in above PL decay spectra results. However, with the gate bias increased to 15V and 20V (maybe exceeding the threshold tunnelling voltage), large amount of excited electrons accumulate on the interface of QDs, producing enhanced electric field intensity within this QDs/ligands/graphene system, and leading to the tunnelling rate's salient increasing. On the other side, the electric field intensity of electroactive ligand device only grows slightly compared with largely enhanced electric field intensity of insulating ligand device. Here comes the question: is it a convincing conclusion that GNM/QDs device with insulating ligand is also a desirable candidate for the gated FET-type photodetector in practice?

Alternatively, the simulation model of GNM with punched periodic nanoholes has been investigated and demonstrated with nearest-neighbor tight-binding (TB) Hamiltonian method to define and describe the graphene lattice[21]. To focus the study on the charge transfer and the influence of the gated FET structure, p-doping GNM channel was modelled as the p-type semiconductor component with ideal 200 meV bandgap (and other GNM property parameters) which operates like a conventional FET device using quasi-fermi levels in classical regime. And the discrete QDs/ligand layer in reality was treated as continuous layer for calculation as shown in the inset image of fig. 3c, where the ligand component was configured as either electroactive or insulating properties. In this electron concentration distribution image, the excited electron accumulating on the n-type-QDs/ligand interface can be driven to p-type GNM channel by the built-in voltage (caused by FET's gate bias) which, at the same time, trapped the holes within the QDs. It is worth noting that, in case of insulating ligand, the device vertically was configured as the p-i-n structure where the tunnelling efficiency is determined by the ligand length due to the same parameters (such as relative permittivity ε_r and trap state density N_t) defined in our simulation work. The simulated transfer current curve suggests that rapid current growth (green and blue curves in fig. 3c) can be obtained in an insulating ligand device when the gate voltage exceeds the threshold voltage and that its current reaches almost the same saturation current with the electroactive counterparts. So to verify the efficiency of charge transfer in practical gated FET-type photodetectors with different ligands, a series of experiments on the photoelectric properties are then carried out.

2.2.2 Photoelectric property of the GNM/QDs FET photodetector. The photoelectric property testing loop is shown in fig. 3d to probe the photocurrent of the device under incident light and different gate voltage (V_G). The experimental result in fig.4a with the transfer characteristic comparison shows the Dirac point shift situation of the different four devices under darkness. The electroactive ligand (Py and PANI) transferred the electrons to the GNM more effectively to cause a larger Dirac point shift and dark (leakage) current compared with the counterpart that exhibits the same phenomenon as described above in simulated results under darkness.

Figure 4.c and d contrast the photocurrent gain of the GNM/QDs devices with different ligands on the same incident light wavelength and luminous density (λ=400nm, ρ=17μW/cm^2). The obvious higher dark/light current ratio can be demonstrated in this experiment as a result of the GNM's current constraint effect. And thanks to this effect, even the photocurrent of the GNM/QDs(OA) device can be observed, whereas in the case of pristine graphene/QDs(OA) device little phenomenon occurs according to previous reported papers[10, 19]. Interestingly, the GNM/QDs(TOPO) device has almost the same saturated photocurrent compared with GNM/QDs(Py)

device and is about fourfold than that of GNM/QDs(PANI) when added the positive gate voltage. It is also worthwhile to note that the photocurrent of these four devices accord with the result of previous PL decay spectra at V_G=0V as shown in fig. 4c and d. In addition, the rapidly increased voltage-sensitive photocurrent of the GNM/QDs(TOPO) device accompanied with the increasing gate voltage can be viewed in fig. 4c, and the threshold tunnelling voltage of this device is estimated for about 2V suggested from our simulated work.

By referring to the energy level alignment diagram[19, 32-34] in fig. 4b, it is clear that, while the low LUMO (lowest unoccupied molecular orbital) electroactive ligands (pyridine and PANI) can transfer the electrons feasibly, the high LUMO electroinertia insulating ligands (OA and TOPO) only drive electrons tunnel from semiconducting QDs to graphene directly. Within this framework, the effective tunnelling barrier can be effectively reduced by increasing gate voltage. Therefore, combining the experimental data and simulated results, it is believed to be arbitrary to claim that electroinertia insulating ligands cannot be used in this hybrid FET photodetector.

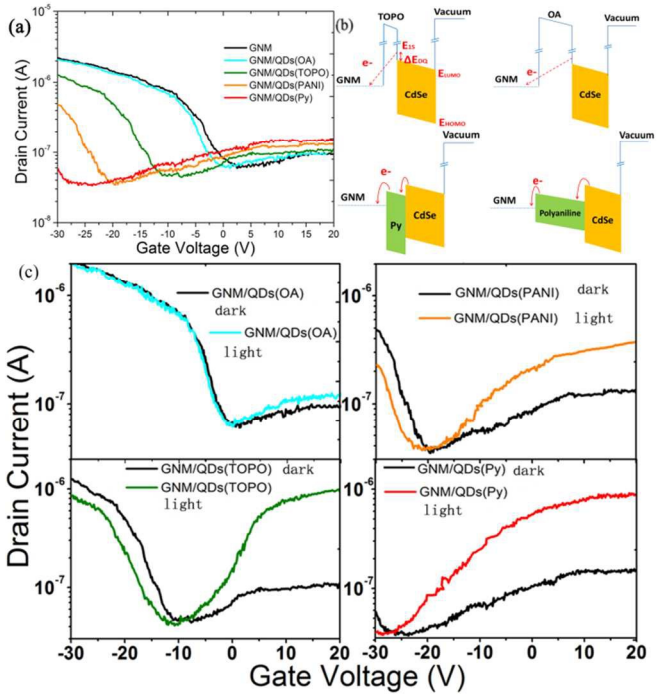

Fig.4 (a) Electric properties measurement of the GNM/QDs FET photodetector without illumination (V_{ds}=30mV). (b) Band alignment diagram of the charger transfer of QDs/ligand/GNM structure. (c) and (d): Transfer character test of the four different samples under the incident 400nm light at 17μW/cm^2 luminous density, and 30mV Drain-Source voltage (V_D)

2.3 Charge tunnelling and transport mechanism and device performance characterization.

2.3.1 Electron transfer efficiency mechanism. Since the photocurrent GNM/QDs(TOPO) device is still 1-2 order of magnitude higher than that of GNM/QDs(OA) device (though they all belong to insulating ligands), and the simulated current difference between the 1.5nm and 2.5nm ligand layer (green and blue curve in fig. 3c) is much smaller than the experiment result. Hence, it is essential to explore the determinant factors in facilitating an effective charge transfer. One obvious reason is that the field intensity (E(V/nm)) in shorter ligand TOPO(~1.5nm) and pyridine(~0.5nm) is larger than their counterparts with longer ligand OA(~2.5nm) and PANI(>2.5nm), which will promote the dynamic charge transfer. But it cannot explain the photocurrent magnitude difference between TOPO and OA, and the only 2 or 3 times photocurrent difference between pyridine and PANI.

In case of tunnelling mechanism (TOPO and OA wrapped devices), because electron on E_{LUMO} (the bottom of conduction band) of QDs has a zero wave vector (k-vector), tunnelling electron that manages to escape from the QDs should at least be at the 1S-state of QDs ($E_{1S} = E_{LUMO} + \Delta E_{QD}$) so that there is enough energy to tunnel through the potential barrier (as shown in the energy level diagram of GNM/QDs(TOPO) in fig.4.b). In order to estimate the escape time for 1S-state electrons of QD, the tunnelling rate K_{tun} is reported[35] to have been applied in a semi-classical approximation as

$$K_{tun} = A f_{QDs} P_{tun}\,, \quad (1)$$

where A, f_{QDs}, P_{tun} is the empirical constant standing for the effective tunnelling area in the surface of QD, electron semi-classical oscillation frequency and quasi-classical probability of tunnelling, respectively.

Among them, f_{QDs}, P_{tun} can be calculated as:

$$f_{QDs} = v_e/2d_{QDs}, v_e = \sqrt{\frac{2E_{1S}}{m_{eff}}} \quad (2)$$

$$P_{tun} = e^{-\frac{2}{\hbar}\int_0^{L_{lig}} dz|p(z)|}, p(z) = \sqrt{2m_{eff}(z)(E_{1S} - U(z))} \quad (3)$$

Where, v_e is the characteristic electron velocity while electron is in the 1S-state, d_{QD} is the QDs diameter, m_{eff} is the effective mass of the electron, $\hbar$ is plank constant, the integral is taken over the tunnel path (L_{lig}, ligand length) going through the potential barrier, $U(z)$ is the electron potential along the tunneling path and $m_{eff}(z)$ is the effective mass of the electron taken along the tunneling path.

This simple model can be used to correspond with the results observed in our experiment. When the length of QDs' encapsulation ligand is increased from TOPO(~1.2nm) to OA(~2.5nm), L_{lig} is increased more than twofold, resulting in rapid weakening of probability of tunnelling P_{tun} due to the exponential relationship between P_{tun} and the L_{lig}'s integral. Besides ligand length, since the effective tunnelling barrier is another impact factor as shown in the formula of p(z), TOPO ligand with advantage of a lower E_{LUMO}(U(z)= E_{LUMO}) also curtailed the effective tunnelling barrier. After the gate voltage reach a threshold value, the photocurrent of the GNM/QDs device will increase tremendously due to the rapidly decreased tunnelling barrier which is described in the experiment of fig. 4c. As for the OA ligand which is considered as a more insulating material, it caused much lower probability of tunnelling P_{tun} due to the exponential manner of these parameters (p(z) and P_{tun}). In our experiment, because the photocurrent of OA device kept a limited level in fig.4c, we suppose that the threshold voltage of OA is too high to reach resulted from the long ligand length and the higher tunnelling barrier (high LUMO). Thus, besides the length difference, the additional tunnelling barrier difference for excited electrons along the tunnelling path of TOPO and OA makes it difficult to configure all the parameters in our simulated model as the real situation, which well explains the relatively large discrepancy between the simulated curve in fig. 3c and experiment curve in fig. 4c:

As for another charge transport mechanism in pyridine and PANI wrapped device, the ligands in these devices operate like an electron transport layer[19]. Thus we ruled out the impact electron tunnelling between QDs and GNM: the influence

factor here should be the field intensity (E(V/nm)), the conductivity and the defects in these material, as predicted and configured in the simulated work. Considering the stronger field intensity, better conductivity and less defects (due to the shorter length and easy ligand exchange process), it is not difficult to understand why the photocurrent of GNM/QDs(Py) is 2-3 times higher than that of GNM/QDs(PANI), and the result that the simulated transfer character curve of different ligand length shows the similar trend compared with the experiment data.

2.3.2 Device response performance characterization.

Fig. 5a depicts the sensitive stable on/off photocurrent (GNM/QDs(TOPO)) of I_D at different gate voltage toward the illumination. Due to free photoinduced electrons transferred from excited QDs to GNM driven by built-in voltage and drifted by the drain-source voltage (V_D), a significant photocurrent increase in GNM/QDs hybrid was found at +4V V_G, where graphene belongs to n-type semiconductor. On the flip side, the photocurrent decrease was obtained at -24V, where hole carriers would be scattered in p-type graphene and the recombination with extra electrons form excited n-type QDs diminished the hole carrier density in GNM channel[31].

High response capability under high speed testing circumstance is another pivotal performance index of the photodetectors. As a consequence, the time-dependent response current to the pulse light signal was probed and the comparison result toward different ligands is shown in fig. 5b. And the detailed time trace response probed voltage variation of TOPO-wrapped and OA-wrapped devices measured by different load resistance (2.5k Ω for TOPO, 20k Ω for OA) and high frequency oscilloscope as shown in figure. S3b. In these dynamic response experiments, the V_D and V_G are fixed on 30mV and 15V, respectively. And the on-state photocurrent rise time can be estimated about 50ms, 15ms, >1s and 0.75s for OA, TOPO, PANI and pyridine wrapped QDs/GNM devices, respectively from the pulse response signal in fig. 5b and 5c. A shorter response time in electron tunnelling ligands device was observed in the time-dependence experiment. After turning on the light, the free excited electrons in QDs will tunnel to the GNM directly without staying in the ligands, while, in the transport mechanism device, many defects and impurities in the ligands will capture the transport electrons and extend the electron exchange time. However, obviously, compared with nanosecond level QDs quenching time, millisecond device response time is much longer. This phenomenon maybe comes from the excited electron accumulation time in QD/ligand interface which will reach a built-in threshold voltage to facilitate the charge tunnelling. It is obvious that the shorter ligand (TOPO) has a much lower threshold voltage for the electron tunnelling[36]. On the other hand, the ligand length should be a very important constant for the electroactive ligands of the devices in dynamic response photocurrent. The electron charge transfer process in vertical structure can be equivalent to the RC oscillation loops to charge for GNM, where the QDs/ligand system can be treated as a parallel circuit with resistance (R) and capacitance (C). The electron charging time is positive correlating to the time constant τ, where $\tau = RC$. And according to capacitance formula: $C = \frac{\varepsilon S}{4\pi k d}$, capacitance will be determined by the distance (ligand length) and ε (dielectric constant). Thus considering the conductivity, ligand length, dielectric constant and lesser defects in pyridine, the response time of GNM/QDs(Py) is shorter compared with that of GNM/QDs(PANI) device.

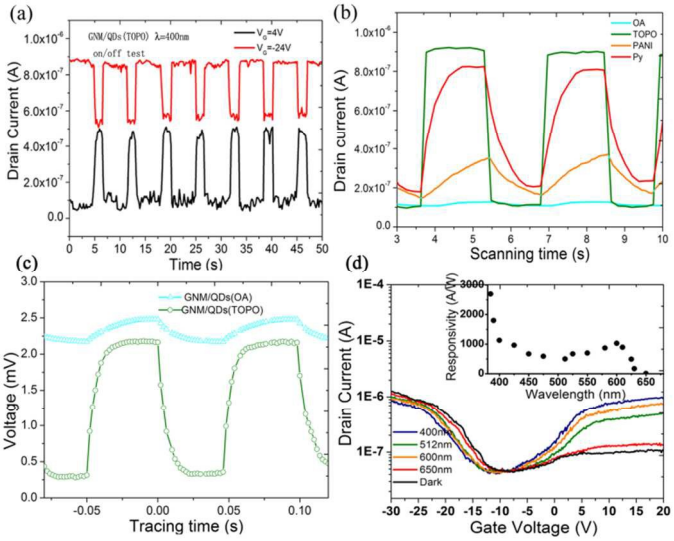

Fig. 5 (a) On/off photoelectric properties of the GNM/QDs(TOPO) photodetector at +4 V and -24 V. (b) The photocurrent on/off response time comparison of the four GNM/QDs devices with different ligands (under 17μW/cm2, 400nm incident light, V_{DS}=30mV). (c) Voltage variation on load resistance in response to on/off illumination experiment in electron tunnelling ligands device (TOPO and OA) for V_{DS}=30mV. (d) The transfer characteristic curve of the GNM/QDs(TOPO) device was measured under 17μW/cm2 luminous density by different wavelengths and the calculated responsivity of this device (inset) at V_G=15V and V_{DS}=30mV.

The responsivity of these devices as well as the response time was calculated under different wavelength illumination. Transfer characteristic curves of GNM/QDs(TOPO) device under some typical wavelengths can be seen in fig. 5d, which shows a fluctuated decrease from violet to red. Since the responsivity(R, A/W) can be calculated from the photocurrent, incidents light luminous density and the effective area. The responsivity of different wave estimated by this formula is shown in the inset image of fig. 5d. As shown in the inset image of fig. 5d, the responsivity of the GNM/QDs follows the same trend compared with the UV-vis spectrum in fig.S1c, where no extra responsivity can be observed outside the absorbance curve. And the responsivity also has a relatively higher value near the emission peak wavelength. Besides, the responsivity of the GNM/QDs FET device with other different ligands is shown in fig. S3d. And the performances of these devices are summarized in table1 and compared with other similar graphene/QDs based photodetectors.

Table 1 Device performance comparison of the different devices

Device structure	ligands	Rise time	On/off ration	Resp. (A/W)	Ref.
GNM/QDs FET	TOPO	15ms	9.1	1800	/
GNM/QDs FET	OA	35ms	1.15	34	/
GNM/QDs FET	Pyridine	0.64s	4.2	1760	/
GNM/QDs FET	PANI	>1s	2.4	574	/
Gra/QDs FET	Pyridine	0.3s	1.15	2700	10
Gra/QDs FET	default	~10s	1.01	8.4A/w	31
Gra/QDs FET	Ethane-dithiol	10ms	~1.5	10^7	37
Gra/QDs vertical-diode	TOPO	0.4ms	10^4	0.5A/w	38
Gra/QDs planar-diode	PANI	~20s	1.005	default	19

3. Conclusions

A GNM/QDs hybrid photodetector was developed with high photocurrent on/off ratio to seek effective charge transfer from quantum dots straightforward. This work was focused on the promotion of the device performance and the mechanism of the effective electron tunnelling. The summary of the devices' performance comparison is concluded in table1. The results revealed the following several scientific interests as: (1) With the current-limiting effect of the p-type GNM, the photocurrent on/off ratio of the FET-type photodetector can be boosted nearly one order of magnitude. (2) By utilizing adequate insulating ligands, the higher photocurrent can be obtained due to the effective electron tunnelling from QDs. (Another shorter ligand insulating Ethane-dithiol ligand has been used in Graphene/QDs hybrid device to replace OA ligands, which also showed an excellent performance[37]) (3) Compared with the electroactive ligand which functions as the electron transport layer, the electron tunnelling across ligand can curtail the response time toward the high-speed pulse light signal. (4) By the analysis of the tunnelling mechanism, built-in field is a crucial factor for the tunnelling probability which also influence the response time of device due to the electron accumulation time in the QDs/ligand interface. We deduced that it is the reason of the longer response time in planar diode or FET device compared with the vertical-diode device. But obviously, to obtain a higher responsivity of photodetectors, FET-type photodetector has unique advantages and it is the guiding significance of our work to find out effective charge transfer method for the future high-performance graphene-based photodetector with high speed, high responsivity, and high on/off photocurrent ratio.

4. Experiment section

4.1 Formation of GNM

4.1.1 Synthesis of Monolayer-graphene. Mono-layer graphene was synthesized by thermal chemical vapor deposition (CVD), which has been reported in detail elsewhere. In overall, 5 sccm CH_4(Air Pcroducts, 99.5%) was aerated to a 50-μm-thick physical vapor deposited Cu foil, at 1000 ° C in an Ar: H_2 ballast(960:40 sccm) at 350mbar for 20min. After a quenching in venting system, the device was cooled down by 2000sccmN_2.

4.1.2 Electrochemical method to form AAO mask. Firstly, aluminium foil (99.99%) was immersed into a mixture solution ($HClO_4$(60 wt%): ETOH=1:4), and then was polished by the Electrolysis method at 20V. Followed is anodizing process for the first time: anode electrode of Al foil and the cathode of Pt mesh were put in a 0.3M oxalic acid (0℃). Thereafter, the mixed solution of phosphoric acid (6 wt%) and chromic acid (1.8 wt%) with Al foil was standing at 75 °C for 10h to avoid the alumina caused by the oxidation. A second time anodizing step was then carried out for half an hour in order to form the sequential porous alumina membrane on Al foil, and saturated $HgCl_2$ solution was used on the surface to exfoliate the AAO membrane. Thereafter, the homologous nanoscale porous AAO with about 40nm hole and 15nm ribbon is produced by 5 wt% phosphoric acid for about 1h. With monolayer CVD-growth graphene transferred to the silica wafer assisted by PMMA film, AAO membrane was fixed on the surface of graphene as the AAO mask.

4.1.3 GNM FET device fabrication and device lifetime. On the graphene/AAO surface, approximately 5nm Ti was deposited by RF sputtering method for about 5s in Ar_2 circumstance (1.5Pa) by a Ti target (99.999%) under room temperature. Next, wet-etching solution (HF and NaOH) was utilized to etching graphene and AAO mask for about 40s to form the GNM silica substrate. To define the FET channel, lithography process was used and Ti(5nm) and Au(50nm) electrode was deposited by thermal evaporation. The as-prepared GNM Si/SiO_2 FET wafer was cut to four pieces for the different four devices with different ligands. The four QDs solution samples (about 3mg/mL, 50μL) were released by micropipette toward the FET channels, respectively and dispersed through a spin coating process with 1000rpm to form an approximately 28nm QDs thin film. And after the 300℃ annealing process to bonding the QDs and GNM channels, the AFM image in fig.2c shows the surface morphology of the QDs film. In previous section, the significant role of the annealing has been discussed. However, the device especially the organic ligands bonding GNM and QDs were exposed to the humid ambient which could influence the performance of the devices after stored for a period of time. As can be seen in figure S4b, the devices can remain stable in first several weeks, but it seems that device wrapped with pyridine ligands dropped firstly because this device is sensitive to the electron transport performance decline of the pyridine. And as we supposed, the TOPO device does not rely on the transport of the organic ligand, in a consequence, this device even showed an excellent performance after stored for three months. Moreover, maybe the thick PANI and OA ligands could prevent this device from the oxidation and damp air and showed a highly stable photocurrent for a long time. Of course, if we can utilize some encapsulation or passivation method for the channel of device in the future, it is not very difficult to produce the FET-type photodetector with better stability.

4.2 Synthesis of QDs and GNM/QDs hybrid.

4.2.1 Ligand exchange of QDs and ligands storage life time. CdSe QDs (diameter: 4.8nm) capped with trioctylphophine oxide (TOPO) and oleic acid (OA) ligands were purchased from Wuhan Jiayuan Quantum Dots CO., LTD, as shown in fig.S1(a). The ligand exchange procedure of QDs capped with pyridine (Py): QDs(OA) solution was heated (70°C, 1 h), and then added to ethanol (volume ratio 1:2). After centrifuging the mixture again, the

collected precipitate was pyridine capped CdSe QDs, which was re-dispersed in toluence by means of sonication for 2 hours at room temperature. And the morphology of the as-prepared QDs (Py) can be seen in the SEM image of fig.S1(b). Two step of synthesizing CdSe (QDs@PANI)[39]:the first step is to prepare tailored QDs: the TOPO ligands capping on the CdSe QDs are exchanged for 4-formyldithiobenzoic acid ligands, which forms a dithioate bridge between the QDs and the ligand; then, to form the polyaniline encapsulation on the CdSe QDs, the aniline tetramer solution was added to the tailored QDs. After the condensation reaction between with the 4-formyldithiobenzoic acid ligands and the tetramer, the aniline tetramer is grafted on the surface of QDs to form the QDs(PANI) as shown in fig.S1(c).

4.3 Measurement and instruments.

The Morphology of the device microstructure is characterized by scanning electron microscope (SEM, Hitachi S4800) and the QDs detail image is characterized by transmission electron microscope (TEM, Tecnai G2 F20 U-TWIN). Photoluminescence intensity and time-resolved spectrofluorometer (FL2-21-IHR320-TCSPC) is carried out to detect the charge transfer in the neutral GNM channel. Keithley 2400 is utilized to character the electric properties of the GNM/QDs FET device. And high performance *Agilent* DSO91204A was used to probe the voltage variation in the high speed time trace experiment. LED lamp source which the different wavelength diode and power can be adjusted was used as the top light-modulated terminal. In addition, the multi-wavelength optic intensitometer DES-100H (U.S.A SP Co.Ltd) was used to confirm the power intensity.

Supporting information

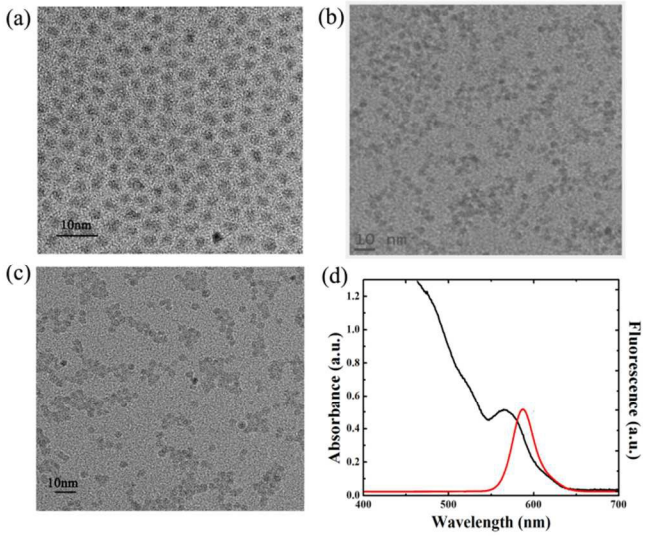

Fig.S1 TEM image of CdSe QDs encapsulated by TOPO (a), Pyridine (b) and polyaniline (c) ligands. (d) The UV-vis absorbance and photoluminescent spectrum of CdSe QDs (TOPO).

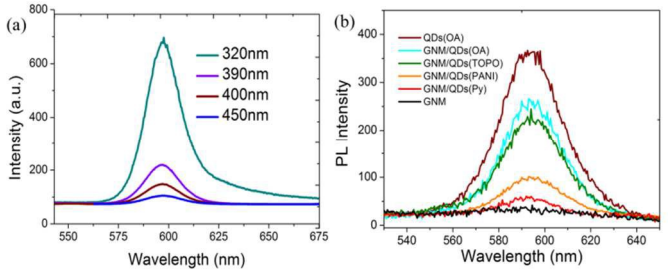

Fig.S2 (a) Fluorescent intensity of the QDs(TOPO) solution under different excited wavelength. (b) Steady-state photoluminescent intensity of the QDs on the GNM silica substrate capped with different ligands.

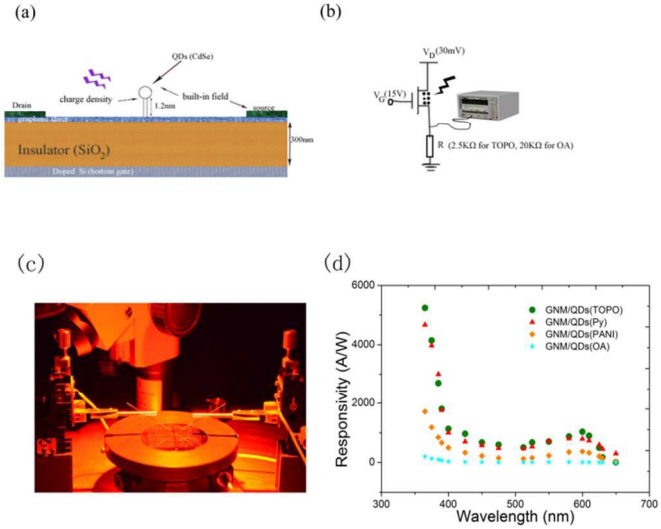

Fig.S3 (a) Schematic of the simulated device structure and the basic parameter in the GNM/QDs FET photodetector. (b) The testing schematic of pulse signal testing through oscilloscope. (c) The Device testing image of the FET device under illumination. (d) The comparison of the GNM/QDs device's responsivity with different ligands under 17μW/cm^2 luminous power density and different wavelength.

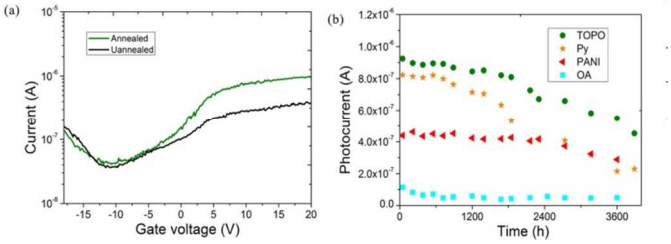

Fig. S4 (a) Voltage-current curves upon annealing and unannealing using four-probe methods for TOPO@QDs device. (b) The performance decline trends for the four different devices.

Acknowledgements

This work was supported in part by National Key Basic Research Program 973(2010CB327705), National Natural Science Foundation Project (51120125001, 51350110232, 61372030, and 51202028), Foundation of Doctoral Program of Ministry of Education (20120092120025), and the Research Fund for International Young Scientists from NSFC (51050110142, 61150110167, and 51150110160).

Notes and references

[a] *Electronic science and engineering school, Southeast University, Nanjing, China. lw@seu.edu.cn.*
[b] *National center for Nanoscience & Technology, Beijing, China. daiq@nanoctr.cn.*
[c] *London Center for Nanotechnology, University College London, London WC1H 0AH, United Kingdom. lichi@nanoctr.cn.*
†Xiang Liu and Nianze Liu are contributed equally to this work.
Electronic Supplementary Information (ESI) available: The TEM image of all the four QDs with different ligands, the PL and UV-vis spectra of QDs and the GNM/QDs with different ligads and the testing device on the probe station under the LED light. See DOI: 10.1039/b000000x/

1 F. Bonaccorso, Z. Sun, T. Hasan and A. C. Ferrari, *Nat Photonics* 2010, **4**, 611-621.
2 Q. Bao, and K. P. Loh, *ACS Nano.*, 2012, **6**, 3677-3694.
3 R.-J. S. Xuetao Gan, YuandaGao, Inanc Meric,TonyF.Heinz, Kenneth Shepard, James Hone, SolomonAssefa and Dirk Englund, *Nat Photonics*, 2013, **7**, 883-887.
4 S.-H. Cheng, T.-M. Weng, M.-L. Lu, W.-C. Tan, J.-Y. Chen and Y.-F. Chen, *Sci. Rep.*, 2013, **3**.
5 S. Heeg, R. Fernandez-Garcia, A. Oikonomou, F. Schedin, R. Narula, S. A. Maier, A. Vijayaraghavan and S. Reich, *Nano Lett*, 2013, **13**, 301-308.
6 L. G. Cançado, A. Jorio, E. H. M. Ferreira, F. Stavale, C. A. Achete, R. B. Capaz, M. V. O. Moutinho, A. Lombardo, T. S. Kulmala and A. C. Ferrari, *Nano Lett*, 2011, **11**, 3190-3196.
7 L. G. De Arco, Y. Zhang, C. W. Schlenker, K. Ryu, M. E. Thompson and C. W. Zhou, *Acs Nano*, 2010, **4**, 2865-2873.
8 J. L. S. Jun, and E. Jang, *Acs Nano*, 2013, **7**, 6310-6320.
9 M. Zhu, X. Li, Y. Guo, X. Li, P. Sun, X. Zang, K. Wang, M. Zhong, D. Wu and H. Zhu, *Nanoscale*, 2014, **6**, 4909.
10 Z. Sun, Z. Liu, J. Li, G.-A. Tai, S.-P. Lau, and F. Yan, *Adv. Mater.*, 2012, **24**, 5878–5883.
11 Z. C. Xiaomu Wang, Ke Xu, Hon Ki Tsang, and Jian-Bin Xu, *Nat Photonics*, 2013, **7**, 888-891.
12 M. Andreas Pospischil, MarcoM.Furchi, Dominic Bachmann, Romain Guider, Thomas Fromherz and Thomas Mueller, *Nat Photonics*, 2013, **7**, 892-896.
13 T. J. Echtermeyer, L. Britnell, P. K. Jasnos, A. Lombardo, R. V. Gorbachev, A. N. Grigorenko, A. K. Geim, A. C. Ferrari and K. S. Novoselov, *Nat Commun*, 2011, **2**, 458.
14 Y. Liu, R. Cheng, L. Liao, H. Zhou, J. Bai, G. Liu, L. Liu, Y. Huang and X. Duan, *Nat Commun*, 2011, **2**, 579.
15 M. Freitag, T. Low, W. Zhu, H. Yan, F. Xia and P. Avouris, *Nat Commun*, 2013, **4**.
16 S. Kaniyankandy, S. Rawalekar and H. N. Ghosh, *The Journal of Physical Chemistry C*, 2012, **116**, 16271-16275.
17 K. Kim, J. Y. Choi, T. Kim, S. H. Cho and H. J. Chung, *Nature*,2011, **476**, 338-344.
18 J. Li , L. Niu , Z. Zheng , and F. Yan, *Adv. Mater,* 2014, **26**, 5239–5273.
19 K. T. Nguyen, D. Li, P. Borah, X. Ma, Z. Liu, L. Zhu, G. Grüner, Q. Xiong, and Y. Zhao, *ACS Appl. Mater. Interfaces*, 2013, **5**, 8105–8110.
20 J. Bai, X.Zhong, S. Jiang, Y. Huang and X. Duan, *Nat nanotech*, 2010, **5**, 190-194.
21 S. Berrada, V. Hung Nguyen, D. Querlioz, J. r. Saint-Martin, me, A. Alarcón, C. Chassat, A. Bournel and P. Dollfus, *Appl Phys Lett*, 2013, **103**, 183509.
22 J.-M. Shieh, Y.-F. Lai, W.-X. Ni, H.-C. Kuo, C.-Y. Fang, J. Y. Huang and C.-L. Pan, *Appl Phys Lett*, 2007, **90**, 051105.
23 C. Y. Chien, W. T. Lai, Y. J. Chang, C. C. Wang, M. H. Kuo and P. W. Li, *Nanoscale*, 2014, **6**, 5303.
24 H. Al-Mumen, L. Dong and W. Li, *Appl Phys Lett*, 2013, **103**, 232113.
25 Y. Y. Hui, G. a. Tai, Z. Sun, Z. Xu, N. Wang, F. Yan and S. P. Lau, *Nanoscale*, 2012, **4**, 3118.
26 M. Wang, L. Fu, L. Gan, C. Zhang, M. Rümmeli, A. Bachmatiuk, K. Huang, Y. Fang, and Z. Liu, *Sci. Rep.*, 2013, **3**.
27 T. Kato, and R. Hatakeyama, *Nature Nanotech.*, 2012, **7**, 651-656.
28 Y. Q. Huang, R. J. Zhu, N. Kang, J. Du, and H. Q. Xu, *Appl. Phys. Lett.*, 2013, **103**, 143119.
29 X. Geng, L. Niu, Z. Xing, R. Song, G. Liu, M. Sun, G. Cheng, H. Zhong, Z. Liu, Z. Zhang, L. Sun, H. Xu, L. Lu, and L. Liu, *Adv. Mater.*, 2010, **22**, 638–642.
30 M. J. Greaney, S. Das, D. H. Webber, S. E. Bradforth, and R. L. Brutchey, *ACS Nano*, 2012, **6**, 4222–4230.
31 D. Zhang, L. Gan, Y. Cao, Q. Wang, L. Qi, and X. Guo, *Adv. Mater.*, 2012, **24**, 2715–2720.
32 J. de Araújo Gonçalves, A. L. D. Ramos, L. L. L. Rocha, A. K. Domingos, R. S. Monteiro, J. S. Peres, N. C. Furtado, C. A. Taft, and D. A. G. Aranda, *J. Phys. Org. Chem.*, 2010, **24**, 54–64.
33 C. Querner, P. Reiss, S. Sadki, M. Zagorska, and A. Pron, *Phys. Chem. Chem. Phys.,* 2005, **7**, 3204.
34 B. S. Kim, M. A. Islam, L. E. Brus, and I. P. Herman, *J. Appl. Phys.*, 2001, **89**, 8127.
35 H. Zhao, Z. Fan, H. Liang, G. S. Selopal, B. A. Gonfa, L. Jin, A. Soudi, D. Cui, F. Enrichi, M. M. Natile, I. Concina, D. Ma, A. O. Govorov, F. Rosei, and A. Vomiero, *Nanoscale*, 2014, **6**, 7004.
36 H. G. Winful, *Physics Reports*, 2006, **436**, 1–69.
37 G. Konstantatos, M. Badioli, L. Gaudreau, J. Osmond, M. Bernechea, F. P. G. de Arquer, F. Gatti, and F. H. L. Koppens, *Nature Nanotech*, 2014, **7**, 363–368.
38 K. K. Manga, J. Wang, M. Lin, J. Zhang, M. Nesladek, V. Nalla, W. Ji, and K. P. Loh, *Adv. Mater.*, 2012, **24**, 1697–1702.
39 C. Querner, P. Reiss, J. Bleuse, and A. Pron, *J. Am. Chem. Soc.*, 2004, **126**, 11574–11582.

